Underwater sound focusing via quasi-three-dimensional gradient-index lens

Seong-Jin Lee,[1,2,*] Jung-Woo Kim,[3,*] Sang-Hoon Kim,[4] Dongwoo Lee,[5,6] Beomseok Oh,[6] Junsuk Rho,[6,7,8,9,†] and Gunn Hwang[10,‡]

[1] *Aerodynamics and Performance Research Team, Korea Aerospace Research Institute, Daejeon 34113, Republic of Korea*

[2] *Department of Aerospace System Engineering, University of Science and Technology, Daejeon 34113, Republic of Korea*

[3] *Department of Naval Architecture, Republic of Korea Naval Academy, Changwon 51698, Republic of Korea*

[4] *Division of Marine Engineering, Mokpo National Maritime University, Mokpo 58628, Republic of Korea*

[5] *Naval Ship Performance R&D Team, Defense Technology R&D Center, Hanwha Ocean, Geoje 53302, Republic of Korea*

[6] *Department of Mechanical Engineering, Pohang University of Science and Technology, Pohang 37673, Republic of Korea*

[7] *Department of Chemical Engineering, Pohang University of Science and Technology, Pohang 37673, Republic of Korea*

[8] *Department of Electrical Engineering, Pohang University of Science and Technology, Pohang 37673, Republic of Korea*

[9] *POSCO-POSTECH-RIST Convergence Research Center for Flat Optics and Metaphotonics, Pohang 37673, Republic of Korea*

[10] *Department of Drone and Mechanical Engineering, Konyang University, Nonsan 32992, Republic of Korea*

(Received 22 December 2024; revised 19 March 2025; accepted 23 May 2025; published 25 June 2025)

Gradient-index lenses, enabled by meta-atoms, have demonstrated effective focusing capabilities in both airborne and submerged environments. However, the current focusing capabilities remain constrained primarily to two-dimensional systems. Here we introduce a quasi-3D gradient-index lens designed for underwater sound focusing. This lens, characterized by a simple yet effective design, features an additional degree of freedom along the axial direction, enabling controlled wave refraction in longitudinal and lateral directions. To achieve this, eigenfrequency analysis and a scattering parameter retrieval method are used to calculate the band structure and characterize the effective material properties. Numerical simulations and experimental validation confirm the efficacy of the lens in focusing underwater sound and highlight its potential for high-resolution sensing, advanced biomedical imaging, and efficient energy harvesting.

DOI: 10.1103/5z2y-d2c3

I. INTRODUCTION

Studying crystal-like and periodic structures at the subwavelength scale has provided a robust platform for revealing previously unexplored physical properties [1–4]. In particular, the controlled manipulation of the refractive index has resulted in the realization of real-world systems for metamaterials, metalenses, and gradient-index (GRIN) lenses, including those exhibiting locally resonant characteristics [5–14]. Building on these findings, significant progress has been made in directing acoustic waves in both air and water with the use of GRIN lenses, which are typically available in two-dimensional (2D) configurations [15–17].

In general, dimensions are defined by the number of axes along which physical quantities are measured independently. While most studies have been centered mainly on 2D structures for sound focusing [18–20], advancements in 3D printing technology and additive manufacturing now enable the creation of complex structures, such as phononic crystal (PC) GRIN lenses and metalenses, thereby extending their functionality to 3D structures. Additionally, the use of high-impedance materials in fabrication extends the applications from airborne to waterborne environments [21–23]. In particular, additive manufacturing has made it possible to produce poroelastic microlattices, broadband flattened Luneburg lenses, and other advanced acoustic components [24–27]. 3D Luneburg lenses, as higher-dimensional systems,

*The authors contributed equally to this work.
†Contact author: jsrho@postech.ac.kr
‡Contact author: hwangun@konyang.ac.kr

demonstrate considerable promise for energy harvesting in acoustic systems [28]. Comparative studies of 2D and 3D acoustic metamaterials have provided valuable insights into lens design, highlighting the unique advantages of 3D structures, especially regarding band structures and stress distributions [29].

Recent studies, such as investigations into acoustic beam splitters [30], flow-permeable metalenses for subdiffraction sound focusing [31], and passive acoustic source detection [32], highlight the expanding potential of these technologies. Ongoing research on underwater acoustic metamaterials [33] and equifrequency contour (EFC) engineering are advancing the control of wave propagation, allowing greater precision in wave steering [34]. These design recipes are essential for achieving more complex wave manipulation tasks.

In this work, we present a quasi-3D GRIN lens that uses dual-axis wave control to enhance underwater sound focusing. Our proposed design, which incorporates a spatially varying refractive index, enables quasiomnidirectional ultrasound focusing in underwater environments. What makes this lens is the modulation of the refractive index in the longitudinal direction, combined with the simultaneous control of lateral wave propagation. These features are characterized by EFCs and are demonstrated numerically through a straightforward structure and efficient material use: stainless steel cylinders sandwiched between cuboidal plates in water domains. To verify the proof of the concept, we built a water tank setup and experimentally captured underwater sound focusing. The study of GRIN lenses has provided valuable insights into acoustic wave manipulation, particularly in 2D configurations where refractive index gradients are engineered to achieve wave focusing. While these studies have successfully demonstrated wave control within a defined plane, their physical implementation inherently extends into three dimensions, influencing the overall wave dynamics. By incorporating axial wave control alongside transverse refraction, this study provides an extended analytical framework that better reflects the full propagation characteristics of acoustic waves. This refined approach has potential applications in underwater sensing, biomedical imaging, and energy harvesting.

II. METHODS

We begin by investigating the band structures of the unit cell, which consists of a cylindrical meta-atom mounted between cuboidal plates, as shown in Fig. 1. This consituent of the quasi-3D GRIN lens is made of stainless steel (SUS304), a high-impedance material characterized by its mass density $\rho_{\text{sus304}} = 8000$ kg/m^3, speed of sound $c_{\text{sus304}} = 5800$ m/s, Young's modulus $E_{\text{sus304}} = 200$ GPa, and Poisson's ratio $\nu_{\text{sus304}} = 0.27$. This leads to a significant reduction in sound penetration, making it well-suited

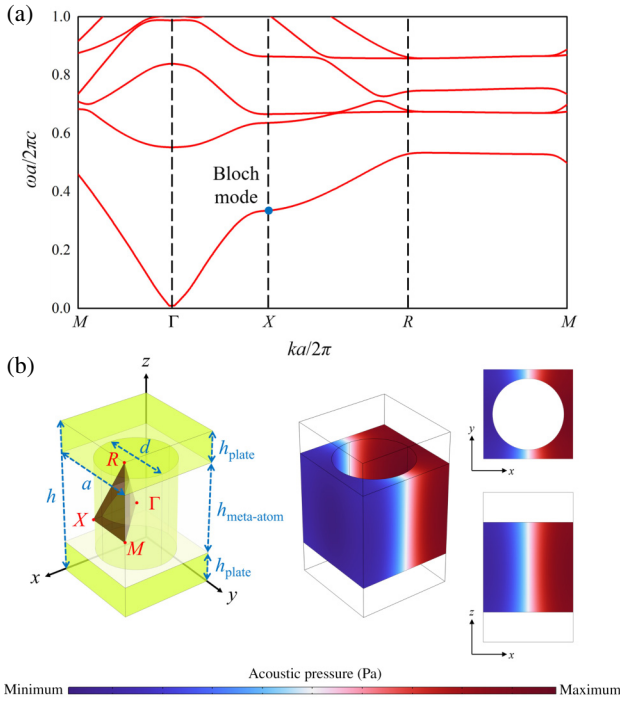

FIG. 1. (a) Band structure of the quasi-3D GRIN lens composed of SUS304 embedded in water. The band structure calculated along the M-Γ-X-R-M path in the irreducible Brillouin zone, with the normalized frequency $\omega a/2\pi c$ plotted as a function of the normalized wave number $ka/2\pi$. (b) On the left is the unit cell, and on the right is the Bloch mode of the acoustic pressure at the point X of the band structure.

for underwater sound focusing applications. The material properties of the background medium (water) are defined by the mass density $\rho = 1000$ kg/m^3 and the speed of sound $c = 1500$ m/s. The geometric parameters are as follows: The diameter d and height $h_{\text{meta-atom}}$ of the meta-atom, and the height h_{plate} of the plates are 2.394, 3, and 1 mm, respectively. The lattice constant a and height $h = h_{\text{meta-atom}} + 2h_{\text{plate}}$ of the unit cell are 3 and 5 mm, respecively.

$$p(\mathbf{r} + \mathbf{a}) = p(\mathbf{r})e^{i\mathbf{k}\cdot\mathbf{a}}, \tag{1}$$

where $p(\mathbf{r})$ is the periodic function of the position vector $\mathbf{r}$, $\mathbf{a}$ is the periodic lattice vector of the structure, $\mathbf{k}$ is the Bloch wave vector, $\mathbf{k}\cdot\mathbf{a}$ represents the phase shift introduced when we move one period along the lattice vector, and $e^{i\mathbf{k}\cdot\mathbf{a}}$ is the complex exponential phase factor. Therefore, $p(\mathbf{r} + \mathbf{a})$ represents the pressure at a position shifted by the lattice vector $\mathbf{a}$ from the original position $\mathbf{r}$ within a periodic structure. In band gaps, wave propagation is forbidden due to the absence of real-valued k components, and the gradient in Γ-X is essential for determining both the refractive index and the wave speed.

In particular, the dispersion relation in a homogeneous medium is given by $\omega(k) = ck/n_{\text{eff}}$, where $\omega(k)$ is the angular frequency as a function of the wave number k, and the effective refractive index n_{eff} can be directly calculated within the range between the points Γ and X. In underwater environments, pressure waves, characterized by compression and expansion resulting from changes in density, dominate over shear waves. Consequently, we leverage this mode for sound focusing with the quasi-3D GRIN lens.

We reveal the quasi-3D nature by examining the EFCs and mapping them to the corresponding n_{eff} density in different planes of wave vector $\mathbf{k}$ space, including the k_x-k_y, k_y-k_z, and k_z-k_x planes, as shown in Fig. 2. These contours provide insight into the wave propagation characteristics of the meta-atoms. Since the group velocity $\mathbf{v_g} = \nabla_{\mathbf{k}}\omega(\mathbf{k})$ is perpendicular to the EFCs in a lossless medium, it indicates the direction of energy flow for the outgoing plane wave. All EFCs are calculated at a frequency of 150 kHz with the packing factor $P_f \sim 0.5$ ($d = 2.394$ mm) of the meta-atom defined by $P_f = V_{\text{meta-atom}}/V$, where $V_{\text{meta-atom}}$ is the volume of the cylindrical meta-atom and V is the volume of the unit cell. We find that the dispersion surface displays inhomogeneous and anisotropic behaviors, which are essential for the design of the quasi-3D GRIN lens, facilitating dual-axis wave control. Notably, the k_x-k_y plane exhibits unique properties in contrast to the k_y-k_z and k_z-k_x planes, emphasizing the quasi-3D nature of the meta-atom structure.

In detail, the EFCs in the k_x-k_y plane with the lowest packing factor P_f appear as perfect circular contours, meaning that waves propagate isotropically in Fig. 3(a). One can define that the radius of the EFCs, denoted as $|\mathbf{k}|$, determines the refractive index. In contrast, as the packing factor P_f increases, the contours take on a squarelike shape with a greater degree of refraction, indicating the emergence of self-collimation effects. Therefore, we can establish a library of refractive indices based on the size of meta-atoms. In Fig. 3(b), the EFCs in the k_y-k_z and k_z-k_x planes exhibit an elliptical contour at $k_x = 0$ (or $k_y = 0$), indicating that waves propagate anisotropically. Otherwise, it shows that the EFCs at $k_x \neq 0$ (or $k_y \neq 0$) are nearly straight lines with less curvature along the k_z direction, showing they are disconnected rather than being smoothly connected as expected. The reasoning behind this mechanism is the impact of the top and bottom plates between the cylindrical meta-atom. The direction of wave propagation is understood by $\partial_{\mathbf{k}}|\mathbf{k}| \propto |k_x| \cdot \mathbf{n}$, which is not permitted in the k_z direction. Consequently, in the x-y plane, waves propagate according to the refractive index profile, whereas in the y-z and z-x planes, their refraction is influenced by the finite structural height, leading to anisotropic wave propagation. Previous studies [15–20] have extensively demonstrated the effectiveness of 2D GRIN lenses in wave focusing, providing a fundamental understanding of refractive index

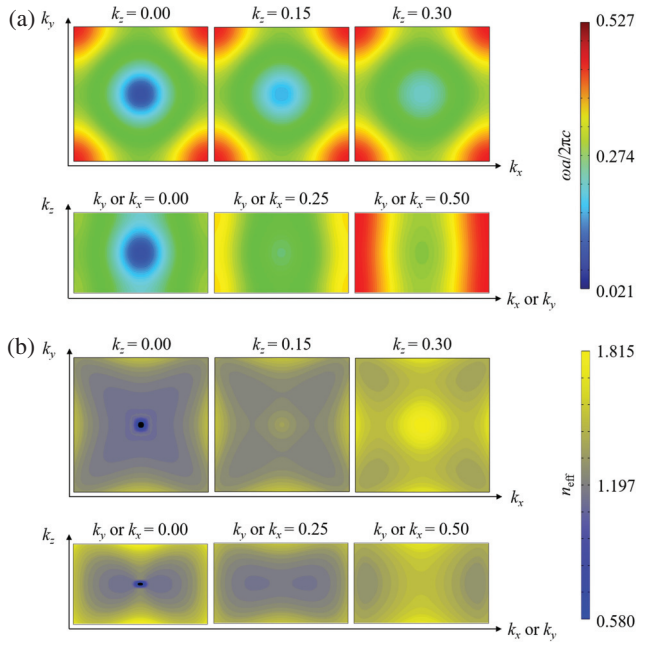

FIG. 2. (a) EFCs of the meta-atom in the k_x-k_y, k_y-k_z, and k_z-k_x planes. (b) Contours of the effective refractive index of the meta-atom in the k_x-k_y, k_y-k_z, and k_z-k_x planes. These contours illustrate the wave propagation characteristics across different planes, offering insight into the anisotropic behavior of the meta-atom in the quasi-3D GRIN lens.

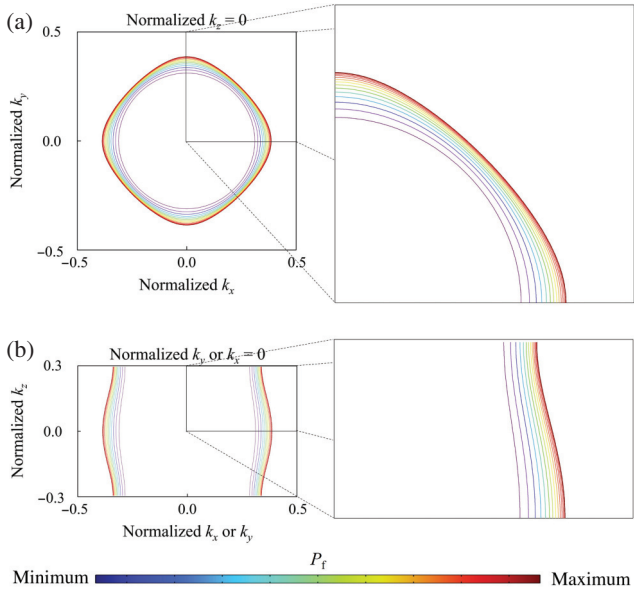

FIG. 3. EFCs of all meta-atoms at a frequency of 150 kHz, forming the quasi-3D GRIN lens. The contours are shown in (a) the k_x-k_y plane and (b) the k_y-k_z and k_z-k_x planes, demonstrating the combined effect of individual meta-atoms in focusing acoustic waves within the lens.

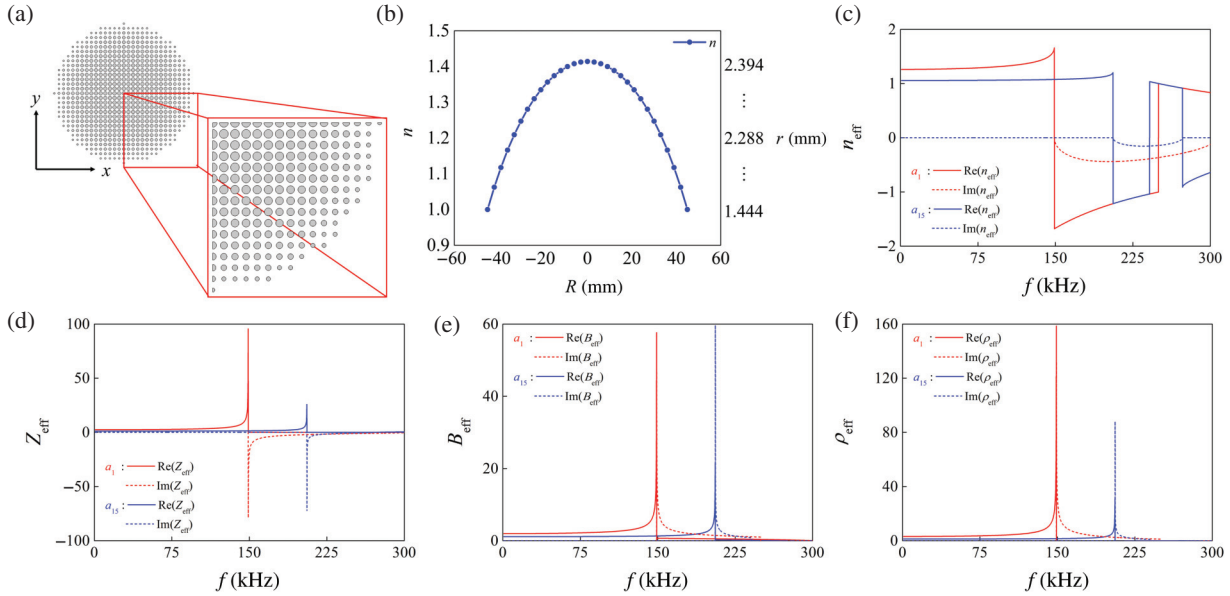

FIG. 4. (a) Quasi-3D GRIN lens in the x-y plane based on the refractive index profile of the Luneburg lens. (b) Relationship between the refractive indices and the size of the meta-atoms. The graphs of the retrieved scattering parameters of the largest and smallest meta-atoms display the effective (c) refractive index n_{eff}, (d) acoustic impedance Z_{eff}, (e) bulk modulus B_{eff}, and (f) mass density ρ_{eff} as a function of frequency, highlighting effective material properties at different frequencies.

modulation. However, in practical realizations, even structures designed for two-dimensional analysis exhibit finite axial dimensions, necessitating a broader interpretation of wave behavior. To account for this, we analyze a Luneburg lens based on a 2D GRIN PC framework while explicitly incorporating axial wave effects, thereby extending the analytical perspective on acoustic wave propagation.

In principle, the Luneburg lens is capable of focusing incoming waves to a focal point on its opposite side without introducing any aberrations. The lens in the x-y plane, designed with a radius of 45 mm, is segmented into 15 concentric layers, allowing a smooth transition in the refractive index profile of the Luneburg lens, as shown in Fig. 4(a). The desired theoretical profile is as follows:

$$n(r) = \sqrt{2 - \left(\frac{r}{R}\right)^2}, \tag{2}$$

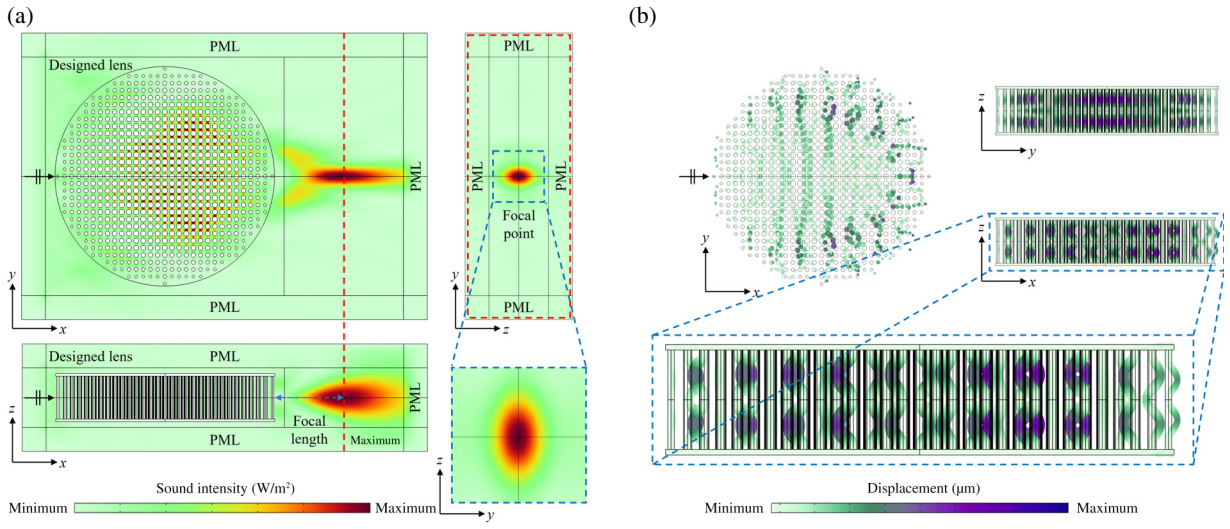

FIG. 5. Numerical simulation of the quasi-3D GRIN lens. Spatial distributions of (a) sound intensity and (b) displacement are shown when the lens is subjected to an incident wave at a frequency of 150 kHz. PML, perfectly matched layer.

where $r = \sqrt{x^2 + y^2}$ is the radial distance and R is the radius of the lens. The relationship between the refractive indices and the size of the meta-atoms is shown in Fig. 4(b). As shown in Eq. (2), the refractive index is $\sqrt{2}$ at the center of the lens, and decreases radially to reach 1 at the edge. Since the volume of the meta-atom is proportional to the refractive index, the meta-atom at the center is the largest, and its volume decreases toward the edge.

We use the scattering parameter retrieval method to assign effective constitutive parameters that correspond to the refractive index profiles in a spatially parameterized manner. This approach involves our evaluating the scattering parameters, namely, the reflection coefficient S_{11} and the transmission coefficient S_{21}, at the boundaries to obtain the effective refractive index n_{eff}, acoustic impedance Z_{eff}, bulk modulus B_{eff}, and mass density ρ_{eff}, expressed as follows:

$$n_{\text{eff}} = \frac{-i \log x + 2\pi m}{ka}, \tag{3}$$

$$Z_{\text{eff}} = \frac{r}{1 - 2S_{11} + S_{11}^2 - S_{21}^2}, \tag{4}$$

$$B_{\text{eff}} = \frac{Z_{\text{eff}}}{n_{\text{eff}}}, \tag{5}$$

$$\rho_{\text{eff}} = Z_{\text{eff}} n_{\text{eff}}, \tag{6}$$

where $x = (1 - S_{11}^2 + S_{21}^2 + r)/2S_{21}$, m is the branch number of the function $\cos^{-1}[(1 - S_{11}^2 + S_{21}^2)/2S_{21}]$, $r = \mp\sqrt{(S_{11}^2 - S_{21}^2 - 1)^2 - 4S_{21}^2}$, k is the wave number of the background medium, and a is the slab thickness (lattice constant) [10]. These material properties are calculated over a frequency range of 0 to 300 kHz, with the highest refractive index observed at around 150 kHz for the largest meta-atom, as shown in Figs. 4(c)–4(f). The bulk modulus indicates resistance to compression as follows: $B = -V(dP/dV)$, where P is the acoustic pressure and V is the volume of the substance. It represents the ratio of the infinitesimal increase in pressure to the resulting relative decrease in volume. The acoustic impedance and the mass density have the following relationships: $Z = \rho c$ and $\rho = m/V$, where c is the speed of sound and m is the mass. Z_{eff}, B_{eff}, and ρ_{eff} are proportional to each other, as shown in Eqs. (5) and (6). That is, the higher the value of these parameters, the greater the resistance to acoustic waves, which ultimately lowers the energy of sound focusing. When a threshold in focusing performance is reached at the frequency of 150 kHz, the meta-atom resonates most effectively, interacting with the incoming acoustic waves. However, at frequencies above 150 kHz, the refractive index becomes negative, leading to phase shifts that adversely affect the focusing performance. Therefore, the retrieved material properties corresponding to the Luneburg-type refractive index profile and the quasi-3D feature are analyzed by EFCs demonstrating both longitudinal and lateral sound focusing.

III. RESULTS

We conduct 3D full-wave simulations, and we find that the designed lens shows significant sound focusing when subjected to incident plane waves at a frequency of 150 kHz, as shown in Fig. 5. During simulations, perfectly matched layers are applied to the outer boundaries to minimize the impact of reflected waves. Thin plates on the top and bottom surfaces of cylindrical meta-atoms in the quasi-3D GRIN lens also guarantee structural stability. We also incorporate acoustoelastic coupling to mimic experimental conditions for the validation of focusing performance. The governing equations of the acoustic wave (Helmholtz equation) and the wave propagation in an elastic medium

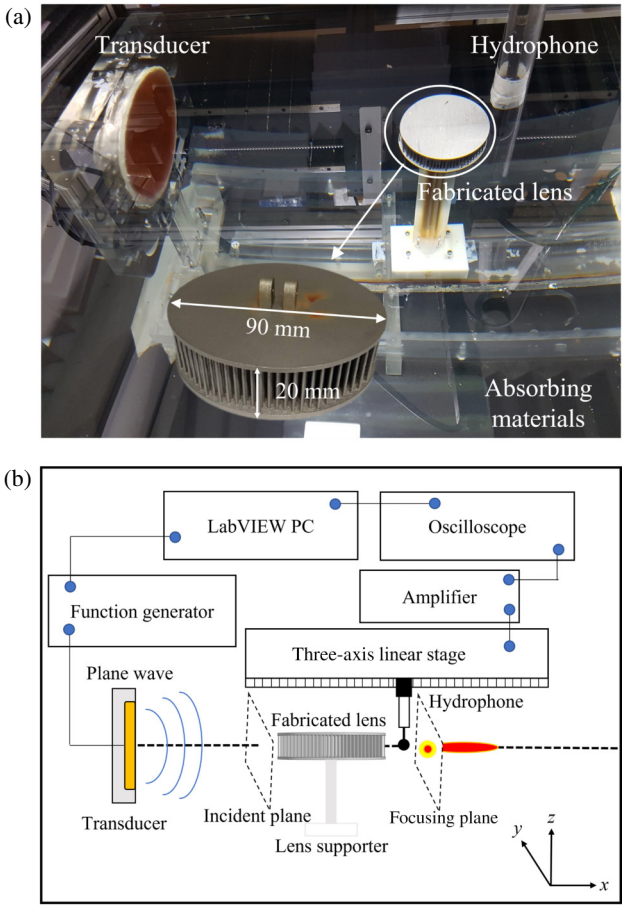

FIG. 6. (a) Experimental setup for validating the focusing performance of the quasi-3D GRIN lens. (b) Schematic diagram showing the placement of the lens and the transducer in the water tank. PC, personal computer.

are as follows:

$$\begin{cases} \nabla^2 p(\mathbf{r}) + k^2 p(\mathbf{r}) = f(\mathbf{r}), \\ \rho(\mathbf{r}) \dfrac{\partial^2 \mathbf{u}(\mathbf{r})}{\partial t^2} = (\lambda(\mathbf{r}) + 2\mu(\mathbf{r}))\nabla(\nabla \cdot \mathbf{u}(\mathbf{r})) \\ \quad - \mu(\mathbf{r})\nabla \times (\nabla \times \mathbf{u}(\mathbf{r})) + \mathbf{f}(\mathbf{r}), \end{cases} \tag{7}$$

where $p(\mathbf{r})$ represents the acoustic pressure at the position vector $\mathbf{r} = [x\, y\, z]^T$. The left-hand side of the first expression in Eq. (7) denotes the spatial distribution and spreading of the wave, and the right-hand side denotes the oscillatory characteristics of the wave according to the medium and the frequency. $f(\mathbf{r})$ and $\mathbf{f}(\mathbf{r})$ represent an external, periodically oscillating source at the position vector $\mathbf{r}$. The left-hand side of the second expression in Eq. (7) represents the inertia of the medium. $\lambda(\mathbf{r})$ and $\mu(\mathbf{r})$ are the Lamé coefficients at the position vector $\mathbf{r}$. $\nabla(\nabla \cdot \mathbf{u}(\mathbf{r}))$ and $\nabla \times (\nabla \times \mathbf{u}(\mathbf{r}))$ are the divergence and the curl of the displacement at the position vector $\mathbf{r}$, respectively. The right-hand side of the second expression in Eq. (7) represents the deformation of the medium as pressure wave and shear waves propagate, respectively. To numerically solve the acoustoelastic coupling in Eq. (7), displacement continuity and stress continuity should be satisfied. The boundary conditions are given by

$$\begin{cases} \mathbf{u} \cdot \hat{\mathbf{n}} = \dfrac{p}{\rho c^2}, \\ \hat{\mathbf{n}} \cdot \boldsymbol{\sigma} \cdot \hat{\mathbf{n}} = -p, \end{cases} \tag{8}$$

where $\mathbf{u}$ is the displacement vector in the elastic domain, $\hat{\mathbf{n}}$ is the unit normal vector at the boundary, $\boldsymbol{\sigma}$ is the stress tensor in the elastic domain, and p represents the acoustic pressure acting as the normal force on the boundary of the solid.

Figure 5(a) clearly illustrates the focusing behavior, which is analyzed in three orthogonal planes—the x-y, y-z, and z-x planes—on the basis of the refractive index profile of the Luneburg lens. In the z-x plane, although the refractive index deviates slightly from that of the Luneburg lens, the acoustic waves are still refracted, as confirmed in Figs. 2 and 3. This leads to quasi-3D focusing, allowing the manipulation of wave fronts across multiple dimensions. In the y-z plane, the focal shape appears elliptical rather than circular due to the anisotropic refractive index distribution, as shown in the EFC analysis in Figs. 2 and 3. The nonuniform distribution of effective wave vectors results in directional variations in phase accumulation, which is directly reflected in the observed focusing pattern. In Fig. 5(b), the bending mode in the x-y plane reveals that the meta-atoms respond dynamically to the incident acoustic wave, leading to controlled refraction along the x axis. Additionally, the coupling between the modes of the meta-atoms and the supporting plates in the y-z and z-x planes dictates the redistribution of acoustic energy. This interaction causes wave refraction not only in the transverse plane but also along the z axis, reinforcing the quasi-3D nature of the focusing process. The spatial distributions of sound intensity and displacement provide further evidence of how the lens governs wave propagation across multiple dimensions, validating its effectiveness in quasi-3D acoustic manipulation.

For the experiments, we construct a water tank setup and fabricate both the lens and the ultrasonic transducer, which are mounted on the bottom of the tank, as shown in Fig. 6(a). The interior of the water tank is coated with sound-absorbing materials to minimize reflections for accurate pressure measurements. The PXI controller (NI PXIe-1062Q chassis with PXIe-6124 multifunction DAQ and PXIe-5413 AWG) with LabVIEW manages the

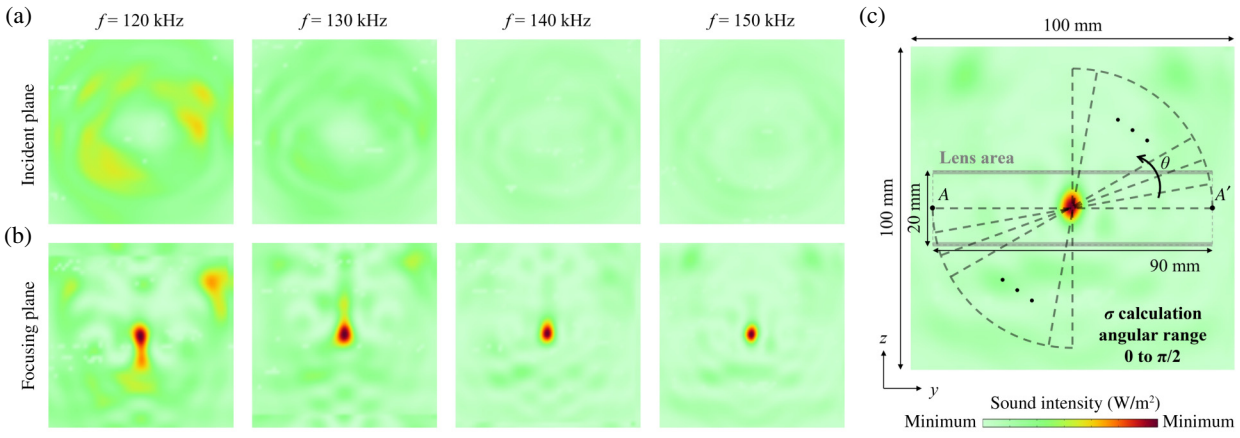

FIG. 7. Experimental results for the focusing performance of the quasi-3D GRIN lens. Spatial distributions of sound intensity in (a) the incident plane and (b) the focusing plane across various frequencies, illustrating the elliptical focal shapes achieved. (c) Measurement range, lens area, and σ calculation angular range by angle θ.

hydrophone (Brüel & Kjær, Type 8105), amplifier (Brüel & Kjær, Type 2693), transducer, and three-axis linear stage (MISUMI, XCVL6300), and its controller (SURUGA SEIKI D520), thereby providing precise control during experimental operations in Fig. 6(b). Underwater sound passing through the fabricated lens is measured with the use of the hydrophone secured to the long rod connected to the three-axis linear stage. As plane waves propagate from the transducer to the fabricated lens, the hydrophone captures pressure data, which are subsequently used for postprocessing.

In Fig. 7, the experimental results demonstrate the focusing performance of the quasi-3D GRIN lens at frequencies of 120, 130, 140, and 150 kHz. To ensure consistent data comparison across different frequencies, sound intensity is normalized for both the incident plane and the focal plane. To quantitatively measure the focusing effectiveness, we define the amplification ratio (AR) as the ratio of the maximum sound intensity in the focal plane to the average intensity in the incident plane. The average intensity is calculated by our integrating the sound power over the area of the incident plane that corresponds to the size of the lens (90×20 mm^2), as shown in Fig. 6. Figures 8(a) and 8(b) illustrate the ARs along the y and z axes, demonstrating the sound focusing capability in different directions through the mechanism of dual-axis control. The AR reaches approximately 10 at frequencies of 140 and 150 kHz. This frequency-dependent behavior is directly related to the effective refractive index distribution of the meta-atoms, as analyzed in Fig. 4. The lens design is optimized for peak focusing efficiency at 150 kHz, and the deviations from this optimal refractive index profile at lower frequencies naturally result in reduced focusing performance.

Furthermore, to explicitly clarify the quasi-3D focusing characteristics of the lens, we conducted additional quantitative analyses based on the angular dependency of the normalized full width at half maximum (σ/λ). Figure 8(c) presents the results for σ/λ measured systematically from 0 (transverse direction) to $\pi/2$ (axial direction), with line AA' and θ as shown in Fig. 7(c). Notably, we observe a clear trend in which σ/λ progressively increases with angle θ, indicating anisotropic wave focusing that results directly from the lens's quasi-3D anisotropic dispersion properties. Specifically, when the angle θ approaches 0, the lens consistently achieves subwavelength acoustic focusing ($\sigma/\lambda < 1$), thus confirming effective wave manipulation capability in the transverse direction. Conversely, when $\pi/2$ is approached (the axial direction), the focal width gradually broadens, reflecting the diminished curvature of the EFCs along the axial wave vector direction (k_z axis). Such angle-dependent focusing characteristics contrast distinctly with the characteristics of fully isotropic 3D systems, which inherently yield uniform focal widths across all directions.

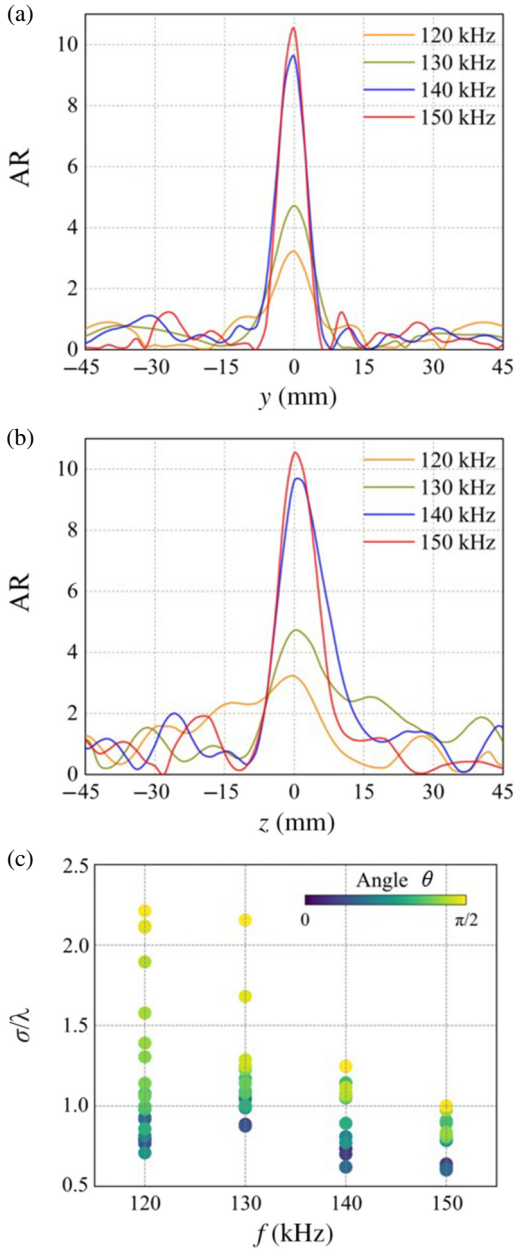

FIG. 8. Experimental results for the AR and σ/λ in the frequency range from 120 to 150 kHz. The AR is plotted as a function of position along (a) the y axis and (b) the z axis. (c) σ/λ as a function of frequency and calculated over the range obtained by our rotating the line AA' of length 90 mm through angle θ from 0 to $\pi/2$, as shown in Fig. 7(c).

Moreover, at the specifically designed operational frequency of 150 kHz, the lens demonstrates subwavelength focusing ($\alpha/\lambda < 1$) at all measured angular orientations, clearly validating the targeted quasi-3D anisotropic focusing mechanism. These additional experimental analyses shown in Fig. 8(c) provide robust, quantitative evidence reinforcing the anisotropic nature and quasi-3D acoustic manipulation capabilities of the

lens as explicitly defined in our study. These findings, consistently supported by the theoretical analyses presented in Figs. 2 and 3 and the experimental data shown in Figs. 7 and 8, collectively substantiate the intended physical mechanism and its operational range. Additionally, the symmetrical patterns observed above and below the focal region at various frequencies [Fig. 7(b)] further indicate the structural influences and anisotropic dispersion characteristics inherent to our lens design. Thus, the present analysis comprehensively addresses the quasi-3D nature of the lens in alignment with our previous definition of dimensionality established in Sec. I.

IV. DISCUSSION

We introduced a quasi-3D GRIN lens for underwater sound focusing, supported by both numerical simulations and experimental findings. Through EFC analysis of the wave behavior of the meta-atoms across multiple planes, we demonstrated the potential for dual-axis control, which can be leveraged in metamaterials for efficient sound manipulation. The quasi-3D structure enabled greater precision in controlling wave propagation along the longitudinal and lateral axes, making it effective and straightforward for a wide range of underwater acoustic applications. The underlying design principle is versatile and can be used in other metamaterial-based systems, offering possibilities for GRIN lenses and beyond.

We recognize that further refinements can be made to extend the scope of this study. As shown in Figs. 2 and 3, the EFC analysis provided insight into the spatial anisotropy of wave propagation, serving as a fundamental indicator of quasi-3D characteristics. Furthermore, both numerical (Fig. 5) and experimental (Fig. 7) results demonstrated that the focal shape deviates from an isotropic circular form, aligning with the anisotropic wave propagation predicted by the EFC analysis. These results collectively support the quasi-3D interpretation of the proposed lens. In particular, the quantitative angular analysis of the focal width (σ/λ) provided strong and direct experimental validation of the lens's anisotropic dispersion and quasi-3D focusing capabilities, distinctly separating our approach from fully isotropic 3D focusing methods. While this study presents a comprehensive analysis of quasi-3D focusing through wave front control and energy redistribution mechanisms, additional investigations into the precise interplay between lens height and plate slab thickness could provide further refinements. Moreover, an extended frequency-domain analysis could offer additional validation of the broadband behavior of the lens in practical underwater applications. However, the current study already establishes a strong foundation for understanding quasi-3D wave manipulation, and the results presented substantiate the core principles governing the designed lens.

Furthermore, the assumption of rigid meta-atoms, which is valid in air, becomes less reliable in water due to smaller impedance contrast and potential structural resonances, even in high-impedance materials such as steel [35]. These considerations could impact acoustic wave transmission and focusing efficiency. We hope that advanced modeling techniques such as topology optimization and artificial intelligence–driven algorithms will be pivotal in accurately predicting and enhancing the focusing performance of metamaterials in water-based environments, thus addressing these challenges and paving the way for innovative designs.

ACKNOWLEDGMENTS

This work was supported by the ICT R&D program for MSIP/IITP (Grant No. 2017-0-00052, "Omni-sensory smart physical sensor original technology for human body sensing and diagnosis"). J.-W.K. acknowledges the academic research project funded by the Ocean Research Institute of the Republic of Korea Naval Academy. J.R. acknowledges the POSCO-POSTECH-RIST Convergence Research Center program funded by POSCO, National Research Foundation (NRF) Grant No. RS-2024-00356928 funded by the Ministry of Science and ICT of the Korean Government, and Grant No. PES4400 from the endowment project "Development of smart sensor technology for underwater environment monitoring" funded by the Korea Research Institute of Ships & Ocean Engineering (KRISO). B.O. acknowledges an NRF Ph.D. fellowship (Grant No. RS-2024-00409956) funded by the Ministry of Education of the Korean Government.

DATA AVAILABILITY

The data that support the findings of this article are not publicly available. The data are available from the authors upon reasonable request.

[1] M. S. Kushwaha, P. Halevi, L. Dobrzynski, and B. Djafari-Rouhani, Acoustic band structure of periodic elastic composites, Phys. Rev. Lett. **71**, 2022 (1993).

[2] W. M. Robertson and J. F. Rudy III, Measurement of acoustic stop bands in two-dimensional periodic scattering arrays, J. Acoust. Soc. Am. **104**, 694 (1998).

[3] Y.-Y. Chen and Z. Ye, Theoretical analysis of acoustic stop bands in two-dimensional periodic scattering arrays, Phys. Rev. E **64**, 036616 (2001).

[4] D. R. Smith, S. Schultz, P. Markoš, and C. M. Soukoulis, Determination of effective permittivity and permeability of metamaterials from reflection and transmission coefficients, Phys. Rev. B **65**, 195104 (2002).

[5] F. Cervera, L. Sanchis, J. V. Sánchez-Pérez, R. Martínez-Sala, C. Rubio, F. Meseguer, C. López, D. Caballero, and J.

Sánchez-Dehesa, Refractive acoustic devices for airborne sound, Phys. Rev. Lett. **88**, 023902 (2001).
[6] B. C. Gupta and Z. Ye, Theoretical analysis of the focusing of acoustic waves by two-dimensional sonic crystals, Phys. Rev. E **67**, 036603 (2003).
[7] S. Yang, J. H. Page, Z. Liu, M. L. Cowan, C. T. Chan, and P. Sheng, Focusing of sound in a 3D phononic crystal, Phys. Rev. Lett. **93**, 024301 (2004).
[8] X. Zhang and Z. Liu, Negative refraction of acoustic waves in two-dimensional phononic crystals, Appl. Phys. Lett. **85**, 341 (2004).
[9] X. Chen, T. M. Grzegorczyk, B.-I. Wu, J. Pacheco Jr., and J. A. Kong, Robust method to retrieve the constitutive effective parameters of metamaterials, Phys. Rev. E **70**, 016608 (2004).
[10] V. Fokin, M. Ambati, C. Sun, and X. Zhang, Method for retrieving effective properties of locally resonant acoustic metamaterials, Phys. Rev. B **76**, 144302 (2007).
[11] Z. He, F. Cai, Y. Ding, and Z. Liu, Subwavelength imaging of acoustic waves by a canalization mechanism in a two-dimensional phononic crystal, Appl. Phys. Lett. **93**, 233503 (2008).
[12] D. Lee, C. Cho, J. Mun, N. Park, and J. Rho, Demonstration of steering acoustic waves by generalized Eaton lens, Appl. Phys. Lett. **113**, 161904 (2018).
[13] B. Oh, K. Kim, D. Lee, and J. Rho, Engineering metalenses for planar optics and acoustics, Mater. Today Phys. **39**, 101273 (2023).
[14] D. Lee, B. Oh, J. Park, S.-W. Moon, K. Shin, S.-M. Kim, and J. Rho, Wide field-of-hearing metalens for aberration-free sound capture, Nat. Commun. **15**, 3044 (2024).
[15] S.-C. S. Lin, T. J. Huang, J.-H. Sun, and T.-T. Wu, Gradient-index phononic crystals, Phys. Rev. B **79**, 094302 (2009).
[16] S. Peng, Z. He, H. Jia, A. Zhang, C. Qiu, M. Ke, and Z. Liu, Acoustic far-field focusing effect for two-dimensional graded negative refractive-index sonic crystals, Appl. Phys. Lett. **96**, 263502 (2010).
[17] T. P. Martin, M. Nicholas, G. J. Orris, L.-W. Cai, D. Torrent, and J. Sánchez-Dehesa, Sonic gradient index lens for aqueous applications, Appl. Phys. Lett. **97**, 113503 (2010).
[18] A. Climente, D. Torrent, and J. Sánchez-Dehesa, Sound focusing by gradient index sonic lenses, Appl. Phys. Lett. **97**, 104103 (2010).
[19] S.-H. Kim, in Proceedings of the 8th International Congress on Advanced Electromagnetic Materials in Microwaves and Optics, Copenhagen, Denmark (IEEE, 2014).
[20] T. P. Martin, C. J. Naify, E. A. Skerritt, C. N. Layman, M. Nicholas, D. C. Calvo, G. J. Orris, D. Torrent, and J. Sánchez-Dehesa, Transparent gradient-index lens for underwater sound based on phase advance, Phys. Rev. Appl. **4**, 034003 (2015).
[21] X. Su, A. N. Norris, C. W. Cushing, M. R. Haberman, and P. S. Wilson, Broadband focusing of underwater sound using a transparent pentamode lens, J. Acoust. Soc. Am. **141**, 4408 (2017).
[22] Y. Ruan, X. Liang, Z. Wang, T. Wang, Y. Deng, F. Qu, and J. Zhang, 3-D underwater acoustic wave focusing by periodic structure, Appl. Phys. Lett. **114**, 081908 (2019).
[23] A. Allam, K. Sabra, and A. Erturk, 3D-printed gradient-index phononic crystal lens for underwater acoustic wave focusing, Phys. Rev. Appl. **13**, 064064 (2020).
[24] G. Kim, C. M. Portela, P. Celli, A. Palermo, and C. Daraio, Poroelastic microlattices for underwater wave focusing, Extreme Mech. Lett. **49**, 101499 (2021).
[25] J.-W. Kim, S.-J. Lee, J.-Y. Jo, S. Wang, and S.-H. Kim, Acoustic imaging by three-dimensional acoustic Luneburg meta-lens with lattice columns, Appl. Phys. Lett. **118**, 091902 (2021).
[26] S. Tong, C. Ren, J. Tao, and L. Jiang, Broadband flattened underwater acoustic Luneburg lens, J. Phys. D: Appl. Phys. **56**, 025102 (2023).
[27] J.-W. Kim, G. Hwang, S.-J. Lee, S.-H. Kim, and S. Wang, Three-dimensional acoustic metamaterial Luneburg lenses for broadband and wide-angle underwater ultrasound imaging, Mech. Syst. Signal Process. **179**, 109374 (2022).
[28] A. Allam, K. Sabra, and A. Erturk, Sound energy harvesting by leveraging a 3D-printed phononic crystal lens, Appl. Phys. Lett. **118**, 103504 (2021).
[29] W. Jin, H. Guo, P. Sun, Y. Wang, and T. Yuan, Numerical investigation of discrepancies between two-dimensional and three-dimensional acoustic metamaterials, Front. Mater. **8**, 759740 (2021).
[30] L. Zhao, Z. Sun, Q. Liu, and C. Bi, Acoustic beam splitter based on acoustic metamaterial Luneburg lens, Phys. Lett. A **472**, 128815 (2023).
[31] L. Fan and J. Mei, Flow-permeable and tunable metalens for subdiffraction waterborne-sound focusing, Phys. Rev. Appl. **19**, 024026 (2023).
[32] L. Zhao, L. Tang, Y. Liu, Z. Sun, Q. Liu, and C. Bi, Passive directivity detection of acoustic sources based on acoustic Luneburg lens, J. Acoust. Soc. Am. **154**, 594 (2023).
[33] E. Dong, P. Cao, J. Zhang, S. Zhang, N. X. Fang, and Y. Zhang, Underwater acoustic metamaterials, Natl. Sci. Rev. **10**, nwac246 (2022).
[34] S. M. Kandil, D. A. J. Bisharat, and D. F. Sievenpiper, Engineering equifrequency contours of metasurfaces for self-collimated surface-wave steering, Phys. Rev. Appl. **21**, 044006 (2024).
[35] N. J. R. K. Gerard, Y. Li, and Y. Jing, Investigation of acoustic metasurfaces with constituent material properties considered, J. Appl. Phys. **123**, 124905 (2018).